Journal of
Materials Chemistry A

Materials for energy and sustainability

Accepted Manuscript

This article can be cited before page numbers have been issued, to do this please use: P. Alonso Sánchez, E. Hvidsten Swensen, K. Thangaian, P. E. Vullum, V. Diadkin, F. Vullum-Bruer, J. Campo, A. M. Svensson, F. H. Cova and M. V. Blanco, *J. Mater. Chem. A*, 2026, DOI: 10.1039/D6TA02278B.

This is an Accepted Manuscript, which has been through the Royal Society of Chemistry peer review process and has been accepted for publication.

Accepted Manuscripts are published online shortly after acceptance, before technical editing, formatting and proof reading. Using this free service, authors can make their results available to the community, in citable form, before we publish the edited article. We will replace this Accepted Manuscript with the edited and formatted Advance Article as soon as it is available.

You can find more information about Accepted Manuscripts in the Information for Authors.

Please note that technical editing may introduce minor changes to the text and/or graphics, which may alter content. The journal's standard Terms & Conditions and the Ethical guidelines still apply. In no event shall the Royal Society of Chemistry be held responsible for any errors or omissions in this Accepted Manuscript or any consequences arising from the use of any information it contains.

ROYAL SOCIETY OF CHEMISTRY

rsc.li/materials-a

View Article Online
DOI: 10.1039/D6TA02278B

ARTICLE TYPE

Low-Temperature Silicon Anodes from Biosilica via $AlCl_3$-Assisted Magnesiothermic Reduction

Pedro Alonso-Sánchez[a*], Emilie Hvidsten Swensen[b], Kesavan Thangaian[b], Per Erik Vullum[c], Vadim Diadkin[d], Fride Vullum-Bruer[e], Javier Campo[a], Ann Mari Svensson[b], Federico Cova[f*], Maria Valeria Blanco[g*]

Silicon is a high-capacity anode material, yet its scalable production from sustainable precursors requires low-temperature and controllable synthesis routes. Diatom-derived SiO_2 provides an abundant biogenic feedstock, but its conversion to silicon by magnesiothermic reduction (MgTR), typically conducted at 600–900 °C, is limited by the highly exothermic nature of the reaction, which induces local overheating, promotes side-phase formation, and often results in incomplete SiO_2 reduction. Here, we elucidate the reaction pathway of $AlCl_3$-assisted MgTR as a strategy to decrease synthesis temperature and improve reduction efficiency. By correlating heating ramp rate, isothermal hold time, and salt-to-silica ratio with phase evolution and crystalline silicon fraction, we identify the parameters governing oxygen abstraction and Si formation. Time-resolved in situ synchrotron X-ray diffraction provides direct insight into the reaction mechanism, revealing the early formation of metallic Al, the transient formation of $MgAl_2Cl_8$ as intermediate, and the subsequent crystallization of Si concurrent with the consumption of metallic Al, thereby suggesting that Al acts as the effective reducing agent. Silicon formation proceeds within a chloride-rich molten phase and is achieved at temperatures as low as 250–300 °C. The crystalline silicon fraction is primarily dictated by heating conditions and $AlCl_3$ content, with optimized parameters maximizing Si fraction while suppressing inactive byproducts. Electrochemical evaluation of graphite–SiO_x electrode blends demonstrates enhanced reversible capacity relative to graphite together with moderate cycling stability, confirming the electrochemical activity of the synthesized material. Overall, this work unveils the mechanistic framework of $AlCl_3$-assisted MgTR and provides synthesis guidelines for the low-temperature conversion of diatom biosilica into silicon-based anode materials.

1 Introduction

The global market for silicon (Si) anodes is forecast to expand rapidly, from USD 327–357 million in 2024 to USD 10–21 billion by 2034, corresponding to compound annual growth rates above 40% across multiple analyses[1–3]. This growth is driven largely by the demand for electric vehicles and the pursuit of higher energy density in lithium-ion batteries (LIBs). Current industrial implementations are based on blending Si into graphite electrodes, providing specific capacities in the range of 1500–2500 $mAhg^{-1}$, a clear improvement over pure graphite (372 $mAhg^{-1}$) but still below the theoretical capacity of Si (3579 $mAhg^{-1}$)[4]. Pushing Si content beyond current industrial limits is a technological necessity[5–8], demanding scalable, low-temperature, and cost-efficient synthesis pathways to produce battery-grade Si from sustainable feedstock[9].

Natural SiO_2 sources such as diatom frustules, clays, zeolites, sand, and agricultural residues offer low-cost and sustainable feedstock for silicon anodes, with inherent advantages including hierarchical porosity and high surface area[10–13]. These features facilitate Li-ion transport and help buffer the large volume changes of Si during cycling, making biogenic templates highly attractive for advanced anode design[14–18]. However, conventional carbothermal reduction, the established industrial route for silicon production, requires high processing temperatures of about 1900°C, which destroys the intrinsic nanostructure and morphology of biogenic templates, thereby limiting its suitability for nanostructured anode design. Magnesiothermic reduction (MgTR, Equation 1) has been proposed as a moderate-temperature alternative (600-900 °C), successfully applied to diverse SiO_2 sources including diatom frustules, clays, zeolites, sand, and agricultural residues[19–27]. Nevertheless, MgTR remains challenging to control: its strongly exothermic nature

[a] Instituto de Nanociencia y Materiales de Aragón (INMA), CSIC-Universidad de Zaragoza, Zaragoza 50009, Spain; E-mail: p.alonso@unizar.es
[b] Department of Materials Science and Engineering, Norwegian University of Science and Technology, Trondheim, NO-7491, Norway.
[c] SINTEF Industry, Trondheim, NO-7491, Norway.
[d] Swiss-Norwegian Beamlines (SNBL) at European Synchrotron Radiation Facilities (ESRF), Grenoble, 38042, France.
[e] SINTEF Energy, Trondheim, NO-7491, Norway.
[f] ALBA CELLS, Cerdanyola del Vallés 08290, Barcelona, Spain; Email: fcova@cells.es
[g] Institut de Ciència de Materials de Barcelona, ICMAB-CSIC, Bellaterra 08193, Catalonia, Spain; E-mail: vblanco2@icmab.es
∗ Corresponding author

View Article Online
DOI: 10.1039/D6TA02278B

induces local hot spots that promote sintering and collapse of fragile nanostructures, while incomplete reduction or local Mg excess/deficiency leads to electrochemically inactive byproducts such as Mg_2Si and Mg_2SiO_4[28–31]. These drawbacks lower the Si yield, complicate purification, and ultimately compromise electrochemical performance.

$$2\,Mg(s) + SiO_2(s) \rightarrow Si(s) + 2\,MgO(s) \quad (1)$$

The use of low-melting $AlCl_3$ ($T_m \approx 192°C$) has recently attracted attention as a means to reduce the effective reaction temperature in metallothermic reductions. Owing to its low melting point, $AlCl_3$ introduces a transient molten-salt environment at temperatures far below conventional MgTR conditions, which can homogenize reactant distribution, facilitate mass transport, and suppress localized overheating. In aluminothermic and zincothermic reductions, this approach has enabled silicon formation at substantially reduced temperatures (200–250 °C)[32–36]. In the context of magnesiothermic reduction, however, the function of $AlCl_3$ remains unclear. Rather than acting as an inert matrix, several studies indicate that the salt actively reshapes the reaction pathway. Reported intermediates such as $MgCl_2$, AlOCl, and $MgAl_2Cl_8$ suggest that chlorine-mediated redox chemistry occurs during MgTR[37,38]. In particular, the in situ formation of metallic Al (Equation 2) has been proposed, implying that reduction may proceed via a secondary aluminothermic step instead of direct Mg–SiO_2 interaction. Concurrently, the formation of $MgAl_2Cl_8$ has been attributed to a cross-reaction between residual $AlCl_3$ and $MgCl_2$ (Equation 3). Despite these hypotheses, direct experimental evidence clarifying the sequence of intermediate formation and their thermodynamic hierarchy is still lacking.

$$3\,Mg + 2\,AlCl_3 \rightarrow 3\,MgCl_2 + 2\,Al \quad (2)$$

$$MgCl_2 + 2\,AlCl_3 \rightarrow MgAl_2Cl_8 \quad (3)$$

More recently, Je et al.[39] proposed a reaction mechanism based on *ex situ* X-ray diffraction and density functional theory (DFT) calculations, in which metallic Mg dissolves in $AlCl_3$ to form metal-$AlCl_3$ complexes that act as reactive intermediates for chlorine transfer. These complexes would destabilize the Si–O bonds in SiO_2 and enable oxygen abstraction via internal Cl^- transfer, leading to the formation of elemental Si along with soluble byproducts such as $MgCl_2$ and AlOCl, rather than solid MgO. These chloride-based byproducts can be removed using mild acid treatments, offering significant advantages in product purification and scalability.

The $AlCl_3$–Mg system also enables SiO_2 reduction to proceed at significantly lower temperatures (~250–300 °C), conditions generally associated with reduced particle sintering, enhanced preservation of the original silica nanostructure, and suppression of undesired Mg_2Si and Mg_2SiO_4 formation. In practice, however, protocols based on this reaction commonly rely on HF etching as a standard post-treatment step to remove residual SiO_2, indicating that the reduction frequently remains incomplete. This dependence represents a major limitation: HF processing introduces substantial environmental and safety concerns and can partially dissolve or structurally alter the newly formed silicon, thereby compromising the structural advantages targeted through low-temperature synthesis.

A rigorous elucidation of the reaction pathway governing $AlCl_3$-assisted MgTR is essential to enable rational control over the process. However, uncovering this pathway is intrinsically challenging because the reduction proceeds within a molten-salt environment, where reactive intermediates nucleate and evolve dynamically and are difficult to capture. Consequently, the $AlCl_3$-assisted MgTR route remains mechanistically ambiguous[40–42], hindering the establishment of predictive design rules necessary to fully exploit this low-temperature strategy for silicon synthesis. Notably, existing interpretations rely almost exclusively on *ex situ* characterization, which does not provide access to the temporal sequence of intermediate formation and phase evolution during the reduction.

In this work, we investigate the $AlCl_3$-assisted MgTR of diatom-derived SiO_2 obtained from industrially cultured diatoms[13] by combining systematic *ex situ* characterization with time-resolved *in situ* synchrotron X-ray diffraction. This integrated approach enables the establishment of a robust mechanistic and parametric framework for the reduction process, elucidating how key synthesis parameters—including heating ramp, salt content, and isothermal holding time—govern the crystalline Si fraction and phase composition. Finally, we show the electrochemical performance of the resulting SiO_x/graphite electrode blends, thereby providing design principles for the scalable synthesis of sustainable, high-performance Si anodes from nanostructured silica.

2 Experimental

2.1 Materials Characterization

Scanning Electron Microscopy (SEM) and Energy-Dispersive X-ray Spectroscopy (EDS) were performed on a Zeiss Sigma 300 instrument to examine particle morphology and elemental composition of both precursor and reduced samples. To minimize charging effects, all specimens were sputter-coated with a thin Au layer prior to imaging.

Ex situ X-ray Diffraction (XRD) was carried out on a PANalytical X'Pert PRO diffractometer equipped with Cu Kα radiation (λ = 1.5406 Å). Rietveld refinement was employed to determine the phase composition and to calculate weight fractions of the post-reduction products. For quantification of crystalline silicon fraction in the acid-washed SiO_x, the powders were mixed with a known amount of corundum (Al_2O_3) as an internal standard, which allowed quantification of the amorphous content.

Nitrogen physisorption was conducted using a Micromeritics ASAP 2020 system. Samples were degassed at 150 °C for 12 h prior to analysis. The specific surface area (SSA) was determined by the Brunauer–Emmett–Teller (BET) method, and the pore size distribution was obtained from the adsorption branch using the Barrett–Joyner–Halenda (BJH) model.

View Article Online
DOI: 10.1039/D6TA02278B

2.2 Molten Salt-Assisted Magnesiothermic Reduction

Amorphous biosilica was obtained from industrially cultured diatom microalgae (Nitzschia sp.[13], Swedish Algae Factory), cultivated under controlled conditions to ensure high purity, morphological uniformity, and reproducibility. Magnesium powder (99%, $< 75\ \mu$m, Sigma-Aldrich) was used as the reducing agent, and anhydrous aluminum chloride ($AlCl_3$, 99%, Sigma-Aldrich) served as the molten-salt.

Reduction reactions were carried out by thoroughly mixing diatom-SiO_2 with Mg and $AlCl_3$ in defined molar ratios. The SiO_2:Mg molar ratio was fixed at 1:2, while the SiO_2:$AlCl_3$ ratio was varied between 1:5 and 1:10 to investigate the influence of salt content. For each *ex situ* experiment, the total reactant mass was 200 mg. The powders were manually ground in an agate mortar and pestle inside an Ar filled glovebox until a homogeneous mixture was obtained. The mixtures were transferred to stainless-steel crucibles with lids and placed in a tubular furnace under continuous Ar flow. Temperature programs were systematically varied to study the effect of heating parameters. Heating rates of 2, 5, and 10 °C/min were employed, followed by isothermal holds at 250 °C for 12–24 h. Representative images of the precursor mixture inside the reactor and the resulting reaction products are provided in Section S2.1 of the Supplementary Information (SI). After thermal treatment, the products were washed with 1 M HCl, filtered, rinsed with DI water and ethanol, and dried at 80 °C under vacuum overnight.

Samples are denoted using the format R–T–S, where R corresponds to the heating ramp rate (2, 5 or 10 °C/min), T indicates the isothermal holding time (12 or 24 h), and S denotes the salt content (L-low or H-high). Details of the reaction parameters are summarized in Table 1.

2.3 *In Situ* Synchrotron XRD of diatom-SiO_2 $AlCl_3$-MgTR

In situ synchrotron powder XRD measurements were performed at BM01 station of the Swiss-Norwegian Beamline (SNBL) of the European Synchrotron Radiation Facility (ESRF, Grenoble, France). A monochromatic X-ray beam with a wavelength of 0.706 Å and a beam size of 100×80 μm was employed. Diffraction patterns were recorded using a Dectris Pilatus 2M direct photon counting area detector. Data acquisition time was of 10 s. The powder mixtures, consisting of diatom-SiO_2, magnesium and $AlCl_3$, were sealed in sapphire capillaries (0.7 mm outer diameter) under inert atmosphere and heated *in situ* using a furnace available at the beamline[43], which was previously calibrated by heating a Si standard and calculating the thermal expansion of the crystal lattice. A LaB_6 powder standard was used for the detector calibration and the instrumental resolution function calculation. Two-dimensional diffraction images were integrated to one-dimensional patterns using the Dioptas software[44]. Sequential Rietveld refinements of the integrated diffraction data were carried out using FullProfApp[45] to analyze the evolution of crystalline phases during the reduction process. The temperature profile was as follows: ramp of 5 °C/min to 250 °C + 30 min holding time at this temperature, followed by heating ramp to 350 °C + 30 min holding time and finally further heating up to 400 °C + 30 min holding time. The sample was then cooled down at 10 °C/min to room temperature. Raw datasets corresponding to this experiment are available at ESRF data portal[46].

2.4 Electrochemical characterization

Electrode slurries were prepared using a Thinky planetary mixer. For the graphite–SiO_x electrodes, the slurry composition consisted of 94 wt% active material (90 wt% graphite, C-NERGY KS6L, and 10 wt% synthesized SiO_x), 2 wt% carboxymethyl cellulose (CMC) binder, 2 wt% conductive carbon (C65), and 2 wt% styrene–butadiene rubber (SBR) in DI water. To enable direct comparison, two baseline electrodes were also prepared with identical additive contents and the same mixing protocol: (i) a pure graphite electrode containing 94 wt% graphite as the sole active material, and (ii) a graphite–SiO_2 electrode with 90 wt% graphite and 10 wt% pristine diatom-SiO_2.

The slurries were cast onto copper foil using a doctor blade with a gap height of 50 μm, followed by drying at 60 °C under vacuum overnight. Circular electrodes with a diameter of 16 mm were punched out and further dried at 120 °C under dynamic vacuum in the antechamber of an Ar-filled glovebox and then assembled into coin-type half cells. Electrode mass loadings were of 1.05 mg·cm^{-2}. Each cell consisted of a working electrode (graphite, graphite–SiO_2, or graphite–SiO_x), a lithium metal foil counter/reference electrode, and a Whatman GF/A glass fiber separator. The electrolyte was 1 M $LiPF_6$ dissolved in a 1:1 (v/v) mixture of ethylene carbonate (EC) and diethyl carbonate (DEC).

3 Results and Discussion

3.1 Pristine diatom-SiO_2 material

A comprehensive characterization of the pristine diatom-derived SiO_2 frustules has been previously reported by the authors[13] and is summarized in Figure S1 of the Supplementary Information (SI). The XRD pattern of the diatom SiO_2 exhibits a broad diffraction feature centered at $2\theta \approx 22.5°$, characteristic of amorphous silica. Nitrogen adsorption–desorption measurements display a type IV isotherm with a pronounced hysteresis loop, indicative of a mesoporous structure. The Brunauer–Emmett–Teller (BET) specific surface area is 69.72 m^2 g^{-1}, with micropore and external surface areas of 23.51 and 46.21 m^2 g^{-1}, respectively, as determined by t-plot analysis. At relative pressures below p/p_0 = 0.2, the isotherm exhibits a concave uptake followed by a gradual slope and a sharp increase approaching p/p_0 = 1, while the desorption branch lies slightly above the adsorption curve due to capillary condensation effects. Scanning electron microscopy reveals elongated frustules (approximately 4 μm wide and 11 μm long) with a highly ordered porous architecture, where circular pores of approximately 70 nm in diameter are uniformly distributed along the frustule walls.

3.2 Effect of hold time, salt ratio and heating rate

The influence of isothermal holding time, salt content, and heating ramp rate on reaction products, silicon yield, specific surface area, and morphological characteristics was systematically investigated. XRD patterns of samples prepared with low (SL) and

View Article Online
DOI: 10.1039/D6TA02278B

Table 1 Sample IDs and synthesis parameters for $AlCl_3$-MgTR of diatom-SiO_2. Reactant ratios (SiO_2:Mg:$AlCl_3$) are given in moles.

Sample ID	SiO_2:Mg:$AlCl_3$	Ramp rate (°C/min)	Hold time (h)	Salt content
R5-T12-SL	1:2:5	5	12	Low
R5-T24-SL	1:2:5	5	24	Low
R5-T12-SH	1:2:10	5	12	High
R5-T24-SH	1:2:10	5	24	High
R2-T24-SH	1:2:10	2	24	High
R10-T24-SH	1:2:10	10	24	High

high (SH) salt content at a fixed heating rate of 5 °C/min, as well as SH samples subjected to different heating ramp rates (2, 5, and 10 °C/min), are shown in Figure 1a and Figure 1c, respectively. The corresponding XRD patterns after acid washing are presented in Figure 1b and Figure 1d. For clarity, samples analyzed prior to acid washing are hereafter referred to as "pre-AW".

Phase analysis of the unwashed samples indicates the formation of typical $AlCl_3$-assisted MgTR reaction products under both SL and SH conditions, including crystalline Si, Al, $MgCl_2 \cdot 6\,H_2O$, and $AlCl_3 \cdot 6\,H_2O$. In particular, elemental Mg was not detected. After AW, the diffractograms reveal the presence of crystalline Si and a broad peak centered at $2\theta \approx 22.5$ °, corresponding to residual amorphous SiO_2. The peak attributed to Al, $MgCl_2 \cdot 6\,H_2O$, and $AlCl_3 \cdot 6\,H_2O$ is no longer observed, confirming their effective removal. A consistent low-intensity peak at $2\theta \approx 45$ °, marked with an asterisk, appears in all AW samples—R5-T12-SL, R5-T24-SL, R5-T12-SH, and R5-T24-SH. This peak does not correspond to any of the known reaction products present before acid washing, suggesting the formation of a minor unidentified phase.

Samples reduced under different heating rates (10, 5, and 2 °C/min) also show characteristic peaks of $AlCl_3 \cdot 6\,H_2O$,$MgCl_2 \cdot 6\,H_2O$, Al, and Si. After acid washing, the patterns are dominated by prominent Si peaks and the same broad feature corresponding to residual amorphous SiO_2. The sample R2-T24-SH, reduced at 2 °C/min, exhibits two additional peaks at $2\theta \approx 26.6$ ° and 45.5 ° that are not associated with any previously identified phases in the pre-AW diffractograms. The samples R5-T24-SH and R10-T24-SH also display the 45° impurity peak, though the 26.6 ° peak is absent. These low-intensity peaks, annotated with asterisks, are not clearly discernible in the pre-AW data due to background noise. To further investigate the origin of the unidentified reflections, several control experiments were performed (see section S2.2 of the SI). The results suggest that the reflections likely originate from residual Al- and/or Cl-containing species, although their low diffraction intensity precludes an unambiguous phase assignment.

Rietveld refinement was performed on samples pre and post-AW for the quantification of the crystalline Si fraction and other post-reduction products. The phase composition of all samples pre-AW is summarized in section S2.3 of the SI. After AW, weight phase percentages show a clear trend with varying parameters as indicated in Table 2. First, fixing the heating ramp to 5 °C indicates that prolonged isothermal holding time and increased salt-to-SiO_2 ratio enhance the crystalline Si fraction, with sample synthesized under SH conditions and 24h holding time showing a 25.52 wt% Si. Among the samples subjected to varying heating ramps under SH conditions and 24h holding time, R2-T24-SH displayed the lowest Si content (19.89%) followed by R5-T24-SH (25.52%) and R10-T24-SH (28.71%), which indicates that a faster heating protocol could favor the SiO_2 reduction. Moreover, analysis of post-AW samples confirmed the effective removal of the main chloride salts and metallic aluminum phases, although minor residual species cannot be completely excluded.

Table 2 Phase compositions of $AlCl_3$-MgTR products post-AW, determined by Rietveld refinement.

Sample ID	Phase wt.% post-AW	
	crystalline Si	amorphous content
R5-T12-SL	16.70	83.30
R5-T24-SL	20.14	79.96
R5-T12-SH	19.31	80.69
R5-T24-SH	25.52	74.48
R10-T24-SH	28.71	71.29
R2-T24-SH	19.89	80.11

The nitrogen adsorption–desorption isotherms for the pristine SiO_2 frustules, R5-T12-SL, R5-T24-SL, R5-T12-SH, and R5-T24-SH are presented in Figure 2a. Up to a relative pressure of $p/p_0 = 0.95$, both low-salt samples exhibit lower adsorption than the precursor. However, beyond this point, the isotherm of R5-T12-SL surpasses that of the precursor, achieving the highest adsorbed gas quantity among the three. All samples show type IV isotherms with hysteresis loops. The isotherms of R5-T12-SH and R5-T24-SH closely resemble those of their low-salt counterparts, confirming the presence of mesoporosity in all samples. Figure 2b presents the SSA distribution derived from the t-plot method. All MgTR-processed samples exhibit lower SSAs compared to the pristine frustules, which display a total SSA of 69.72 m^2g^{-1}—comprised of 46.21 m^2g^{-1} external and 23.51 m^2g^{-1} micropore area. For R5-T12-SL, the total SSA is reduced to 44.66 m^2g^{-1} (28.38 mg^2g^{-1} external, 16.28 m^2g^{-1} microporous), while prolonging the isothermal hold time to 24 h (R5-T24-SL) further decreases both components to 26.12 m^2g^{-1} and 12.56 m^2g^{-1}, respectively. These results indicate a progressive loss of surface area with extended heat treatment under low salt conditions.

The high-salt samples, R5-T12-SH and R5-T24-SH, exhibit similar micropore areas of 15.06 and 15.44 m^2g^{-1}, respectively—lower than the precursor's value. However, in contrast to the low-salt series, the external surface area increases with extended holding time: R5-T24-SH exhibits 37.73 m^2g^{-1} compared to 26.05 m^2g^{-1} for R5-T12-SH. This inverse trend suggests that salt content critically influences the evolution of surface area during MgTR.

In terms of BET surface area, both R5-T12-SL and R5-T24-SL show reduced values (44.66 and 38.68 m^2g^{-1}, respectively)

View Article Online
DOI: 10.1039/D6TA02278B

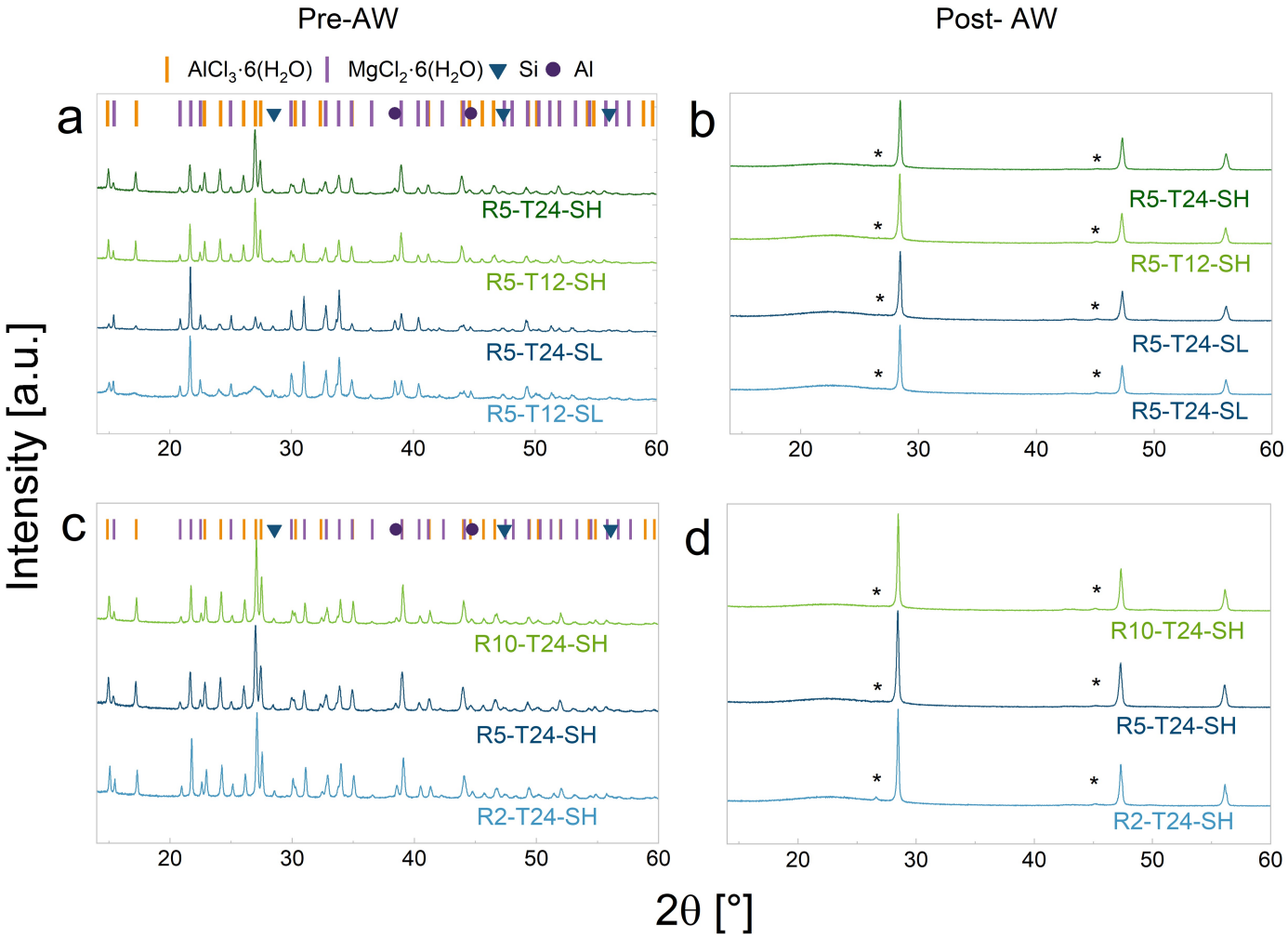

Fig. 1 XRD patterns of $AlCl_3$–MgTR products: a,b) R5-T12-SL, R5-T24-SL, R5-T12-SH and R5-T24-SH pre-AW (a) and post-AW (b); c,d) High salt samples R2-724-SH, R5-T24-SH, and R10-T24-SH before (c) and after (d) AW.

compared to the pristine frustules. A corresponding decline is observed in cumulative mesopore surface area, which decreases from 39.21 m^2g^{-1} in the precursor to 15.38 m^2g^{-1} and 16.98 m^2g^{-1} for the 12 h and 24 h samples, respectively. The average mesopore diameter increases significantly upon processing—49.02 nm and 29.49 nm for R5-T12-SL and R5-T24-SL, respectively—suggesting coalescence or collapse of smaller pores during reduction, particularly under prolonged heating. Under high salt conditions, R5-T12-SH exhibits a total SSA of 41.10 m^2g^{-1} and a mesopore surface area of 13.47 m^2g^{-1}. Extending the hold time to 24 h increases both values to 53.17 m^2g^{-1} and 28.65 m^2g^{-1}, respectively—an opposite trend to that observed in the low-salt series.

Figure 2c presents the nitrogen isotherms of samples synthesized under different heating ramp rates. All exhibit type IV isotherms with hysteresis at $\frac{p}{p_0} > 0.9$. Figure 2d displays the corresponding SSA distribution, revealing that micropore area remains relatively constant (16 m^2g^{-1}) across all ramp rates, while external surface area increases with faster heating: 24.82, 37.73, and 43.25 m^2g^{-1} for R2-T24-SH, R5-T24-SH, and R10-T24-SH, respectively. This trend indicates that a faster heating ramp promotes external surface development during reduction. BET and BJH data (Table 3) further support this observation: total SSA increases with ramp rate, reaching 59.35 m^2g^{-1} for R10-T24-SH, compared to 53.17 m^2g^{-1} and 40.76 m^2g^{-1} for R5-T24-SH and R2-T24-SH, respectively. Similarly, cumulative mesopore surface area increases from 15.23 m^2g^{-1} (2 °C/min) to 28.65 m^2g^{-1} (5 m^2g^{-1}) and 33.54 m^2g^{-1} (10 °C/min). In contrast, the average mesopore diameter decreases with increasing ramp rate, from 39.94 nm at 2 °C/min to 23.44 nm at 5 °C/min and 24.17 nm at 10 °C/min. This suggests that faster heating leads to finer mesopores and greater external surface area.

Figures 2e-h present TEM analysis of selected post-AW samples, illustrating the influence of salt content and thermal parameters on microstructure and phase composition. Figure 2e shows HAADF-STEM images of the R5-T24-SL sample, synthesized with low salt content. This sample consists of three main components: amorphous SiO_2 frustules, amorphous SiO_x, and crystalline Si. Compared to the other samples, it contains a higher fraction of residual SiO_2 and a lower relative content of SiO_x ($x < 1$) and crystalline Si. STEM-EELS/EDS mapping confirms the coexistence of these phases, and EDS quantification of SiO_x particles in the

View Article Online
DOI: 10.1039/D6TA02278B

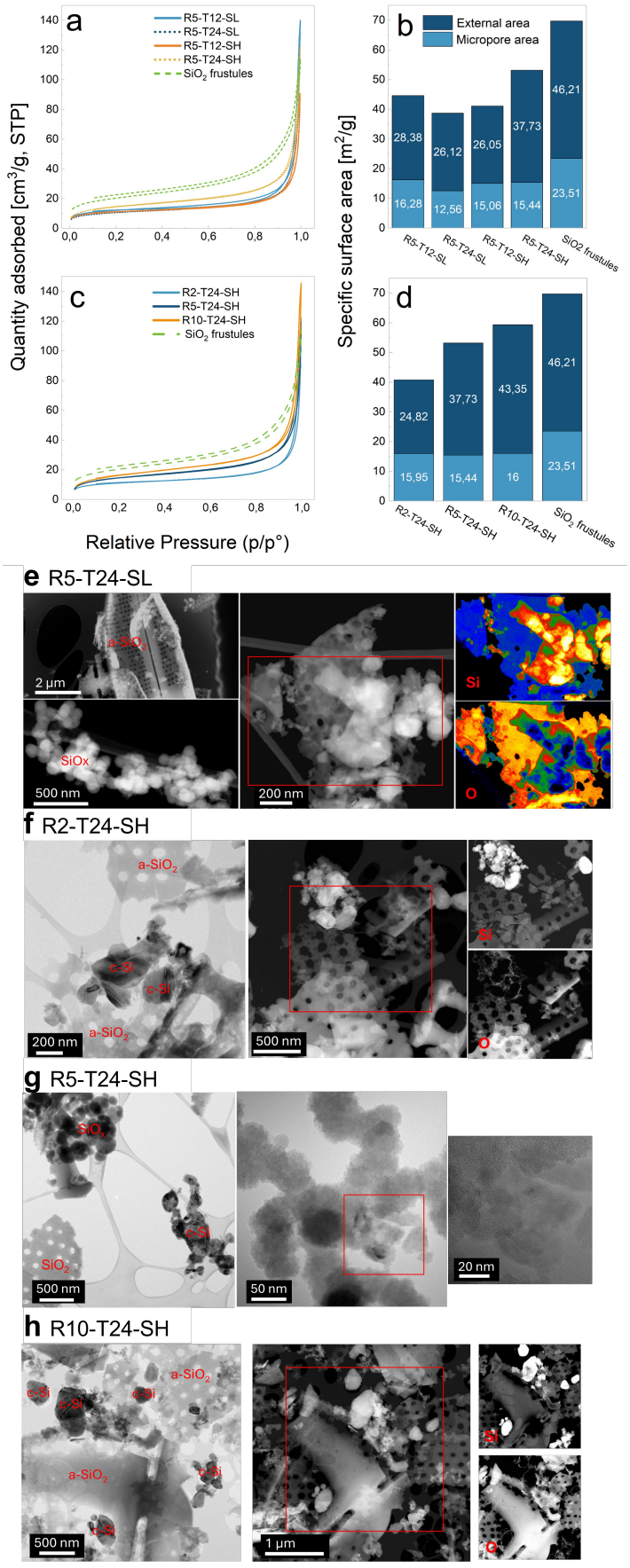

Fig. 2 N_2 physisorption and microstructural characterization of post-AW $AlCl_3$–MgTR products: (a–d) Adsorption–desorption isotherms and corresponding external and micropore surface area contributions for R5-T12-SL, R5-T24-SL, R5-T12-SH, R5-T24-SH and R2-T24-SH, R5-T24-SH, R10-T24-SH. (e–h) TEM images of selected samples: (e) R5-T24-SL, (f) R2-T24-SH, (g) R5-T24-SH, and (h) R10-T24-SH.

View Article Online
DOI: 10.1039/D6TA02278B

Table 3 N_2 physisorption results for samples synthesized under varying hold times, salt contents and heating ramp rates.

Sample ID	SSA $[mg^2g^{-1}]$	Cumulative mesopore surface area $[mg^2g^{-1}]$	Avg. mesopore diameter [nm]
SiO_2 frustules	69.72	39.21	15.61
R5-T12-SL	44.66	15.38	49.02
R5-T24-SL	38.68	16.98	29.49
R5-T12-SH	41.10	13.47	38.90
R5-T24-SH	53.17	28.65	23.44
R10-T24-SH	59.35	33.54	24.17
R2-T24-SH	40.76	15.23	39.94

mapped region yields an average composition of 74 at.% Si, 23 at.% O, 2.3 at.% Cl, and 0.8 at.% Al. By contrast, Figure 2f displays bright-field TEM images of the R2-T24-SH sample, prepared with high salt content and the slowest ramp rate. This sample contains only amorphous SiO_2 particles and crystalline Si particles, with no evidence of composite domains (i.e., Si nanocrystals embedded in an amorphous matrix). Elemental mapping (EELS and EDS) of the red-framed region confirms Si and O as the main constituents, along with surface-localized carbon, while Mg, Al, and Cl are absent.

Figure 2g shows the results for the R5-T24-SH sample, prepared with a high salt content and a moderate heating ramp. The sample contains amorphous SiO_2 frustules, amorphous SiO_x ($x < 1$), and crystalline Si. The magnified region reveals the presence of small Si nanocrystals embedded within an amorphous SiO_x ($x \ll 1$) matrix, indicative of partial composite formation. Figure 2h presents bright-field TEM images of the R10-T24-SH sample, synthesized under the highest ramp rate. Similar to the slow-ramp counterpart (R2-T24-SH), this sample contains only amorphous SiO_2 and crystalline Si particles, with no evidence of composite domains. Elemental maps from the red-framed STEM region confirm Si and O as the dominant elements, with only trace amounts of Al and no detectable Mg or Cl. Taken together, these observations highlight that composite formation is highly sensitive to the heating ramp and salt content, with intermediate conditions favoring the partial embedding of crystalline Si within an amorphous SiO_x matrix. At this point, it is worth noting that the apparent preservation of the precursor morphology, is associated with the fraction of material that remains unreacted or only partially reduced. In contrast, regions where crystalline Si particles are formed do not retain the original morphology. This behavior agrees with previous studies on $AlCl_3$-assisted reductions, where silica undergoes structural disintegration prior to the Si crystallization[39,47,48].

3.3 Reaction mechanism by in-situ synchrotron XRD

Due to the low Si yield obtained after the $AlCl_3$-MgTR, time resolved in-situ synchrotron XRD measurements were performed to elucidate the reaction mechanism. The same reactant stoichiometries as those used in the previous sections (SiO_2:Mg:$AlCl_3$ molar ratios of 1:2:5 and 1:2:10) were employed to investigate the effect of the SL and SH concentrations.

An initial *in situ* experiment was conducted to define appropriate measurement conditions and temperature protocols, as shown in Figure S4 of the SI. The sample was first heated to 220°C and held isothermally, followed by a second isothermal step at 250°C and a final heating stage to 300°C, where the temperature was maintained for 2 h. Analysis of the diffraction data revealed that an isothermal step of 30 min was sufficient for phase evolution to stabilize at each temperature. Moreover, a markedly higher reaction progress was observed between 250 and 300°C, identifying this interval as critical for the reduction process. Since the *in situ* measurements are specifically designed to investigate the reaction dynamics and phase evolution, the thermal protocol initially explored the same synthesis temperature used in the *ex situ* experiments (250°C), and was subsequently extended stepwise to 400°C, with isothermal holding times of 30 min, in order to expand the explored temperature range and gain further insights into the reaction pathway. Nevertheless, the key mechanistic events of the reduction occur within the temperature range investigated under *ex situ* conditions.

3.3.1 Low salt conditions

Figure 3 presents the results of the study under SL conditions. The evolution of the diffractograms collected during the experiment, together with the corresponding heating protocol, is displayed in Figure 3a and b, respectively. Rietveld refinement was employed to quantify the phase weight fractions throughout the experiment. However, the pronounced asymmetry observed in the $AlCl_3$ (020) reflection (see Figure S5 of the SI), prevented a reliable refinement at the early stage of the reaction. Consequently, Rietveld refinement was only performed once the $AlCl_3$ had completely melted, as shown in Figure 3c and d. A more detailed discussion about this issue is provided in Section 3.2 of the SI. Based on the evolution of the main Bragg reflections, the reaction mechanism can be divided into four distinct stages, separated by dashed lines and marked with different colors in the images.

Initial heating stage. During the first stage, Bragg peaks associated with crystalline $AlCl_3$ and Mg are clearly visible in the diffractograms, while the amorphous SiO_2 lacks long-range order, therefore appearing as a broad intensity feature at $2\theta \approx 10^\circ$. No evidence of reaction is observed in this stage.

Molten salt activation. The second stage is characterized by the onset of Al reflections and the decrease in intensity of Mg peaks, indicating the reaction between $AlCl_3$ and Mg, which leads to the formation of the mixed salt $MgAl_2Cl_8$ as an intermediate phase and $MgCl_2$ as the final product. From 100°C onward, trace amounts of $MgAl_2Cl_8$ are detected. However, the formation of this phase rapidly accelerates as the temperature approaches the $AlCl_3$ melting point. When intensity of $AlCl_3$ reflections starts to decrease, a transient signal of diffuse scattering emerges, indicating that the salt is entering its molten state. Subsequently, this signal progressively decreases while $MgAl_2Cl_8$ rapidly crystallizes. At ≈175°C the absence of $AlCl_3$ reflections indicates that the salt has either completely reacted with Mg to form Al and $MgAl_2Cl_8$ or has entered the molten state. Between this temperature and ∼220°C, the formation of metallic Al continues, while the mixed salt reaches its maximum weight fraction (84.7%). Upon further heating up to 235°C, $MgAl_2Cl_8$ is rapidly consumed, leading to the formation of $MgCl_2$, while Mg content continues to de-

View Article Online
DOI: 10.1039/D6TA02278B

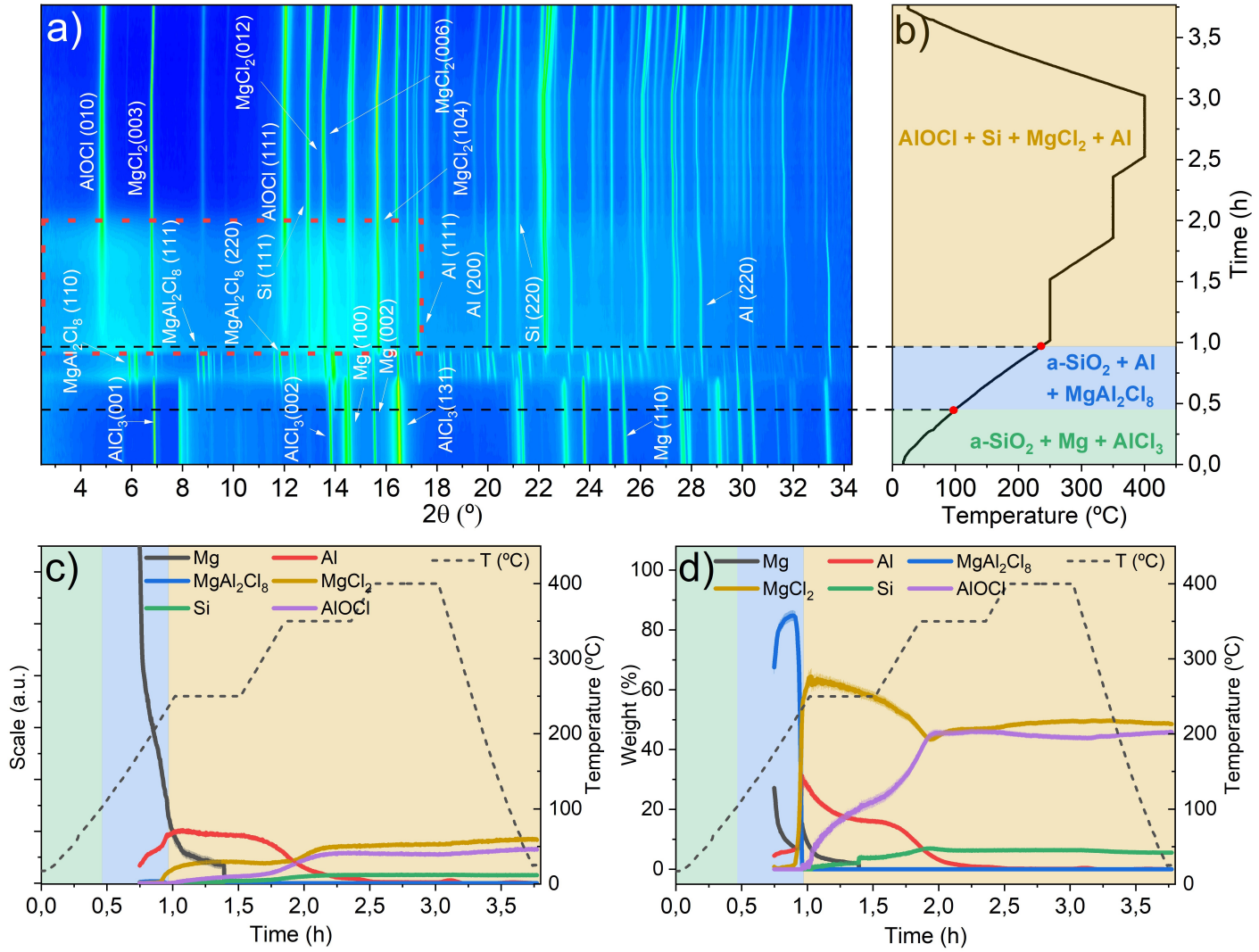

Fig. 3 In situ study of $AlCl_3$-MgTR under SL conditions: (a) time-resolved diffraction data, (b) corresponding heating protocol, (c) refined scale factors of the detected crystalline phases (d) corresponding phase weight fractions. Dashed lines and shaded regions delineate the distinct reaction stages. The red dashed box highlights the region where the diffractograms exhibit strong diffuse scattering.

crease and metallic Al rises once again. Simultaneously, a pronounced increase in the diffuse background intensity is observed (as marked with a dashed box in Figure 3a), which is consistent with the formation of a molten phase. At the end of this stage, the weight concentration of crystalline phases is 57% $MgCl_2$, 30% Al and 13% Mg. An example of Rietveld refinement of one diffractogram collected during this stage is shown in Figure S6 of the SI.

SiO_2 reduction. In this stage, the partial reduction of the amorphous SiO_2 precursor and the crystallization of Si take place, while the temperature profile includes three 30 min holding steps at 250, 350 and 400°C, followed by a cooling ramp down to room temperature. During the first holding step (250°C), Si and the final byproduct AlOCl slowly crystallize, as indicated by the evolution of their refined intensities in Figure 3c, while metallic Al is consumed to a minor extent and $MgCl_2$ content remains essentially unchanged. It is worth noting that phase weight concentration graph may not fully reflect the actual phase evolution since some phases that were not previously detected (such as molten or amorphous phases) become detectable at this stage. Therefore, for a correct interpretation, the refined scale factors and phase weight graphs (Figure 3c and d) should be analyzed simultaneously. Upon further heating up to 350°C, the reduction reaction accelerates, leading to a more pronounced formation of Si, AlOCl and $MgCl_2$, together with the total consumption of the metallic Al. In addition, once 350°C is reached, the strong diffuse scattering signal disappears, which indicates the consumption of the molten phase formed at the end of the previous stage. From this temperature onward, no significant reaction signal is observed. Moreover, during the cooling ramp, no crystallization of $AlCl_3$ is detected, confirming the complete consumption of the salt during the reaction. An example of Rietveld refinement of one diffractogram collected during this stage is shown in Figure S7 of the SI. A simple mass balance shows that the crystalline products detected by in situ XRD (Si, AlOCl and $MgCl_2$) cannot account for all Al and Cl introduced as $AlCl_3$. This indicates that a fraction of the Al/Cl

View Article Online
DOI: 10.1039/D6TA02278B

inventory remains in a noncrystalline reservoir (molten or amorphous chloride species) and/or redistributes along the sealed capillary through the gas–condensed equilibrium of $AlCl_3$, potentially condensing in cooler regions outside the XRD sampling volume.

3.3.2 High salt conditions

Figure 4 summarizes the *in situ* study conducted under SH conditions. The contour plot shown in Figure 4a, together with the corresponding heating protocol in Figure 4b allows the evolution of the reaction components to be followed throughout the entire experiment. The results of the Rietveld refinement are summarized in Figure 4c and d, where the refined scale factors and the phase weight concentration of each phase are displayed, respectively. As in the low salt study, Rietveld refinement was performed once $AlCl_3$ had completely melted. Unlike the SL study, the reaction under SH conditions can be divided into four distinct stages. While the overall reaction pathway is similar to that observed in the SL experiment, with the transient formation of $MgAl_2Cl_8$ and the temporal correlation between metallic Al consumption and Si crystallization, significant differences are found in the products formed during the reaction.

No signal of reaction is observed during the *initial heating* stage. When the temperature is further increased up to ∼125°C, within the *molten salt activation* stage, the first indications of $MgAl_2Cl_8$ formation appear. At ∼170°C, the formation of the mixed salt accelerates, leading to the crystallization of metallic Al and the partial consumption of Mg, indicating no significant difference in the activation onset temperature compared to the SL case. From this temperature to 235°C, the mixed salt disappears from the diffractograms, while metallic Al continues to form, Mg is further consumed and a strong diffuse scattering signal emerges in the background, as indicated by the red box of Figure 4a. Therefore, the *molten salt activation* stage follows essentially the same reaction pathway as in the low salt experiment, with one notable difference: no crystallization of $MgCl_2$ is observed by the end of this stage. The *SiO_2 reduction* stage also follows a similar pathway. During the first holding step, at 250°C, Si and AlOCl reflections slowly emerge while metallic Al is progressively consumed. This process further accelerates upon heating up to 350°C, beyond which no significant reaction signal is detected. Moreover, the scattering signal associated with the molten phase persists throughout the entire reduction stage. Upon cooling, reflections corresponding to a new crystalline structure abruptly emerge at 230°C, while the diffuse scattering signal disappears, indicating the crystallization of a previously molten phase. Importantly, this phase is not residual $AlCl_3$, but is instead consistent with the $MgAl_2Cl_8$ structure, confirming the complete consumption of the salt during the reaction. However, its quantification is not possible since it crystallized as a polycrystalline phase rather than as a powder phase, as shown in Figure S8 of the SI. It should be mentioned that under these SH conditions, the Al and Cl supplied by $AlCl_3$ exceed the amount that can be accommodated in the crystalline phases detected by XRD. The excess is therefore attributed to a chloride-rich molten or amorphous reservoir that gives rise to the diffuse scattering observed at high temperature and only partially crystallizes upon cooling.

3.3.3 Reaction pathways and mechanistic framework

The *in situ* studies presented above provide the first time-resolved evidence of the reaction pathway of the $AlCl_3$-MgTR, enabling direct tracking of the SiO_2 reduction process and revealing mechanistic features that could not be resolved by previous *ex situ* approaches. In particular, the early formation of metallic Al prior to Si crystallization, together with the persistence of a chloride-rich molten phase throughout the Si formation step, highlights the highly dynamic reaction environment. While a chlorine transfer mechanism has been proposed in a previous study[39], the present results suggest that, if operative, this pathway would involve the consumption of the metallic Al generated during the molten salt activation stage, rather than the Mg acting as the active reducing species. Notably, under both SL and SH conditions, Si crystallization ceases once metallic Al is fully consumed, despite Al not being expected to act as an effective reducing agent at such low temperatures. This behavior underscores the critical role of the chlorine-rich molten phase in lowering the effective reaction temperature and sustaining Si formation. A further mechanistic finding concerns the origin of the mixed salt $MgAl_2Cl_8$. Contrary to previous assumptions[38], $MgAl_2Cl_8$ does not form via a cross reaction between $AlCl_3$ and $MgCl_2$. Instead, the *in situ* data demonstrate that it is the first crystalline phase to emerge during the *molten salt activation* stage, under both SL and SH conditions, forming directly through the interaction between $AlCl_3$ and Mg. This temporal sequence provides strong indications that $MgAl_2Cl_8$ acts as intermediate in the generation of metallic Al.

To further probe the role of metallic Al in the reaction pathway, and to detect when the reduction of SiO_2 starts, an additional *in situ* experiment was performed under SH conditions, using crystalline SiO_2 as precursor (see Section S3.5 of SI). Unlike the amorphous SiO_2, using the crystalline precursor enables direct monitoring of SiO_2 consumption through its diffraction reflections. Results from this experiment show the concurrent consumption of metallic Al and crystalline SiO_2, providing additional evidence that supports the participation of metallic Al during the reduction.

Finally, comparison between SL and SH conditions highlights the influence of $AlCl_3$ content on the evolution of intermediate species and final products. As previously mentioned, $MgAl_2Cl_8$ disappears at temperatures of approximately 235°C, indicating a transition to a molten chloride-rich phase. This behavior is consistent with the reported $AlCl_3$-$MgCl_2$ phase diagram, which shows a pronounced depression of the melting temperature near 67 mol% $AlCl_3$, corresponding to the stoichiometric composition of $MgAl_2Cl_8$[49].The evolution of the molten phase strongly depends on the $AlCl_3$ content. Under SL conditions, the system shifts away from this $AlCl_3$-rich composition during heating, promoting the formation of $MgCl_2$ and metallic Al. In contrast, under SH conditions the higher $AlCl_3$ content keeps the system within the $AlCl_3$-rich regime, enabling the recrystallization of $MgAl_2Cl_8$ upon cooling.

View Article Online
DOI: 10.1039/D6TA02278B

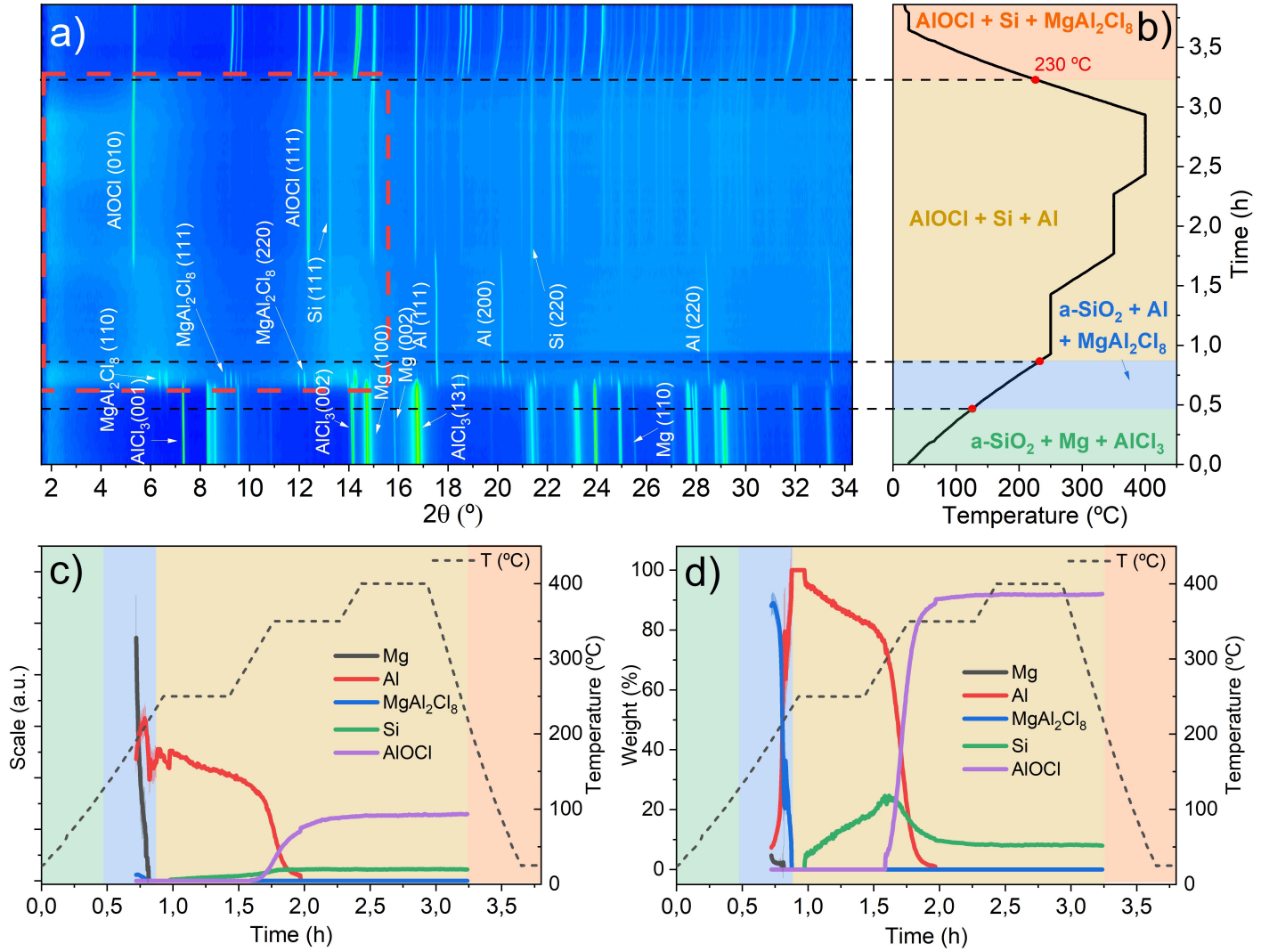

Fig. 4 In situ study of $AlCl_3$-MgTR under SH conditions: (a) time-resolved diffraction data, (b) corresponding heating protocol, (c) refined scale factors of the detected crystalline phases (d) corresponding phase weight fractions. Dashed lines and shaded regions delineate the distinct reaction stages. The red dashed box highlights the region where the diffractograms exhibit strong diffuse scattering.

3.4 Electrochemical performance

The electrochemical performance of the synthesized SiO_x materials, corresponding to the samples characterized ex situ, was evaluated in graphite-blended electrodes and benchmarked against pure graphite and a graphite–SiO_2 (Figure 5a,b). A wt.% ratio of 10/90 (SiO_x/Gr) was selected to test the synthesized material under an industrially relevant configuration. Graphite delivered an initial coulombic efficiency (ICE) of 84.5 % and a formation-cycle lithiation capacity of 384 $mAhg^{-1}$. Incorporation of SiO_2 slightly increased the capacity to 395 $mAhg^{-1}$ but reduced the ICE to 79.1 %, likely reflecting irreversible Li consumption associated with conversion and alloying reactions [14,50].

Gr–SiO_x electrodes exhibited markedly higher initial lithiation capacities (460–518 $mAhg^{-1}$; Figure 5c–g, Table 4). This capacity enhancement was accompanied by a reduction in ICE (77.6–81.7 %), with samples containing higher crystalline Si fractions (R10-T24-SH and R5-T24-SH) showing the lowest ICE values, indicative of increased irreversible reactions during SEI formation and the first alloying cycle. In contrast, R5-T12-SH and R2-T24-SH, with the lowest Si content, exhibited the highest ICE (81.7 %).

After 50 cycles, the reversible capacities of the Gr–SiO_x electrodes stabilized between 314 and 342 $mAhg^{-1}$. R5-T12-SH and R5-T24-SH retained 68.4 % and 67.2 % of their initial lithiation capacities, respectively, and maintained capacities above that of graphite (331 $mAhg^{-1}$). In contrast, R10-T24-SH and R2-T24-SH exhibited faster capacity decay and dropped below the graphite baseline within 20–30 cycles, highlighting the trade-off between Si content and cycling stability. All electrodes reached coulombic efficiencies above 99.8 % after 30 cycles, while graphite achieved the highest CE after 50 cycles (99.98 %), closely followed by R5-T12-SH (99.93 %).

Differential capacity (dQ/dV) analysis (Figure S10 of the SI) supports these conclusions. While Gr and Gr–SiO_2 showed only graphite-related features, Gr–SiO_x electrodes exhibited additional peaks at 0.04 V and 0.45 V associated with the lithiation and

View Article Online
DOI: 10.1039/D6TA02278B

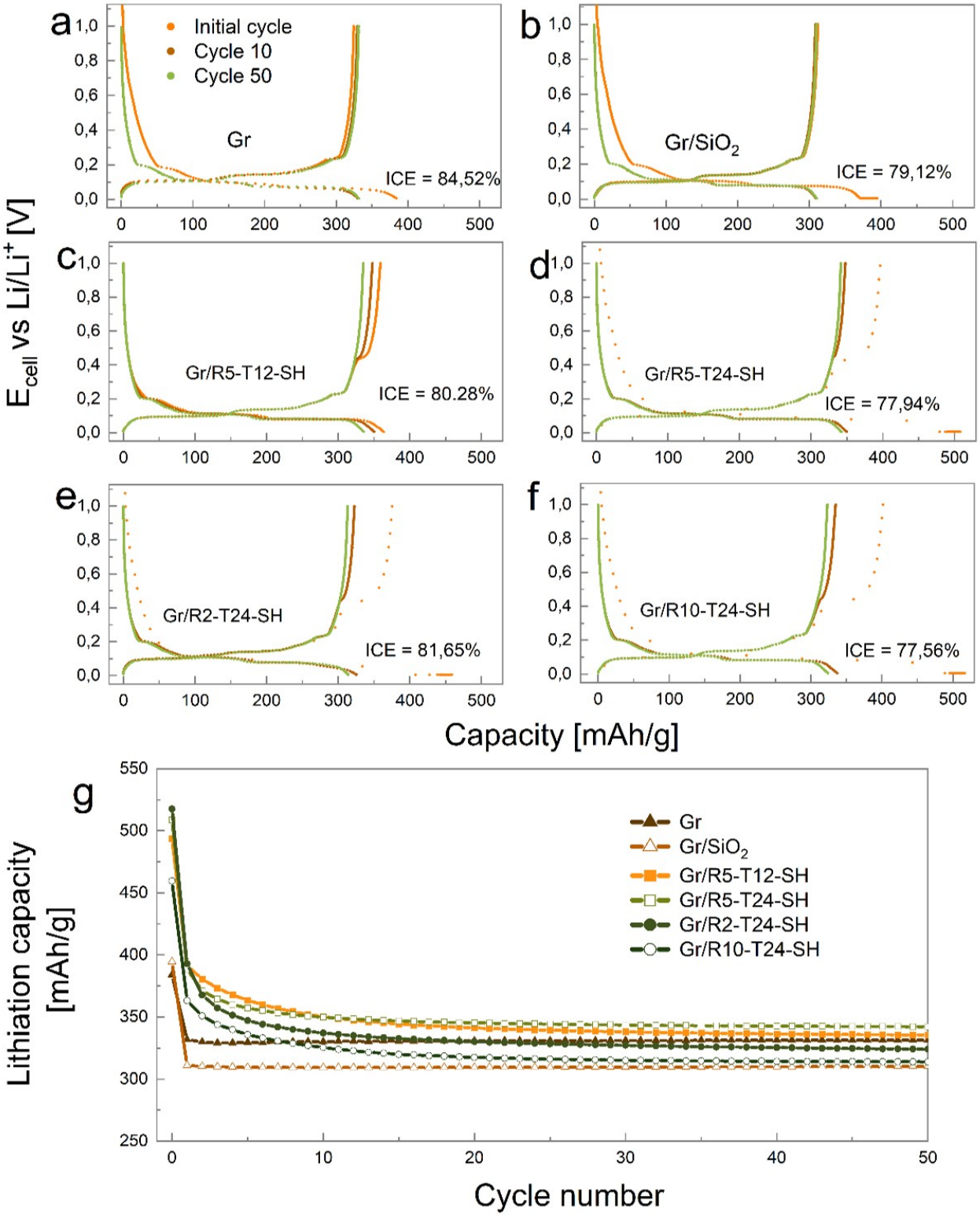

Fig. 5 Voltage profile curves of: a) Gr, b) Gr/SiO_2, c) Gr/R5-T12-SH, d) Gr/R5-T24-SH, d) Gr/R2-T24-SH, e) Gr/R2-T24-SH, and f) Gr/R10-T24-SH electrodes for formation cycle, cycle 10, and cycle 50. g) Evolution of lithiation capacity against cycle number for all electrodes (a-f)

View Article Online
DOI: 10.1039/D6TA02278B

Table 4 Summary of electrochemical performance, for baseline electrodes and Gr–SiO_x electrodes. The Si yield of each SiO_x material added for reference.

Sample ID	Si [wt.%]	ICE [%]	cycle 1	cycle 10	cycle 50
Gr	-	84.52	384	330	331
Gr-SiO_2	-	79.12	395	309	310
R5-T12-SH	19.31	80.28	494	350	336
R5-T24-SH	25.52	77.94	509	350	342
R10-T24-SH	28.71	77.56	518	337	324
R2-T24-SH	19.89	81.65	460	325	314

delithiation of crystalline $Li_{15}Si_4$. These features progressively weakened and disappeared by 30 cycles, indicating early formation but rapid electrochemical deactivation of crystalline Si. The more persistent $Li_{15}Si_4$ signal observed for R2-T24-SH is consistent with its faster capacity decay. Overall, R5-T12-SH and R5-T24-SH deliver the most balanced performance.

The observed electrochemical trends appear to be influenced by the structural properties and phase composition of the synthesized SiO_x material. In particular, the higher initial capacity correlates with the higher crystalline Si fraction, and it is also associated with a lower ICE. However, this enhancement cannot be exclusively attributed to the crystalline Si fraction, since contributions from the amorphous content, different surface area, and irreversible reactions occurring during lithiation of SiO_2 particles may also play an important role. The present data do not allow to disentangle all these contributions. These results nevertheless confirm the activity of the synthesized SiO_x material when incorporated into SiGr blended electrodes.

4 Conclusions

This work provides a mechanistic and parametric framework for $AlCl_3$-assisted magnesiothermic reduction (MgTR) of diatom-derived biosilica and its application in silicon-based anodes for lithium-ion batteries. By systematically varying heating ramp rate, isothermal holding time, and salt-to-silica ratio, we demonstrate that silicon yield and structural preservation are governed by the combined effects of thermal history and molten-salt chemistry.

Time-resolved *in situ* synchrotron X-ray diffraction provides important insights into the $AlCl_3$-MgTR reaction mechanism. The results show the early formation of metallic Al and later consumption, and the persistence of a chlorine-rich molten phase throughout Si crystallization, enabling SiO_2 reduction at temperatures as low as 300 °C. The mixed salt $MgAl_2Cl_8$ is identified as the first crystalline intermediate, forming directly from the interaction of $AlCl_3$ with Mg and acting as a precursor to metallic Al generation. These findings support that the Si formation proceed through the previously reported chlorine transfer mechanism, but with metallic Al acting as the effective redox-active species rather than Mg.

Ex situ structural analysis shows that extended holding times and higher $AlCl_3$ contents increase crystalline Si yield, while faster heating ramps promote higher external surface area and finer mesoporosity. Importantly, only intermediate synthesis conditions favor the formation of Si nanocrystals embedded in an amorphous SiO_x matrix, which provides an optimal balance between electrochemical activity and structural stability.

Electrochemical evaluation of Gr-SiO_x composite anodes confirms the electrochemical activity of the synthesized powders. Materials containing moderate crystalline Si fractions (20-25 wt%) and preserve mesoporosity exhibit the most favorable electrochemical response, delivering CE above 99.8% after moderate cycling time. In contrast, samples with higher crystalline Si fraction show faster capacity fading, suggesting that electrochemical performance is influenced by multiple structural factors.

Overall, this study demonstrates that the performance of biosilica-derived SiO_x is not dictated by silicon content alone, but by the interplay of crystallinity, surface area, and impurity phases controlled through synthesis parameters. By combining *in situ* mechanistic insights with systematic structural and electrochemical analysis, this work establishes clear design principles for $AlCl_3$-assisted MgTR, advancing a low-temperature and scalable route for sustainable silicon anode materials.

Author contributions

Pedro Alonso-Sánchez: Conceptualization, Data curation, Formal analysis, Investigation, Supervision, Methodol- ogy, Validation, Writing – original draft, Writing – review and editing. **Emilie Hvidsten Swensen:** Conceptualization, Data curation, Formal analysis, Investigation, Methodology, Validation, Writing – review and editing. **Kesavan Thangaian:** Investigation, Methodology, Writing – review and editing. **Per Erik Vullum:** Formal analysis, Inves- tigation, Validation, Writing – review and editing. **Vadim Diadkin:** Resources, Writing – review and editing. **Fride Vullum-Bruer:** Funding acquisition, Validation, Writing – review and editing. **Javier Campo:** Funding acquisition, Supervision, Validation, Writing – review and editing. **Ann Mari Svensson:** Funding acquisition, Supervision, Validation, Writing – review and editing. **Federico Cova:** Conceptualization, Data curation, Investigation, Supervision, Validation, Writing – original draft, Writing – review and editing. **Maria Valeria Blanco:** Conceptualization, Funding acquisition, Investigation, Supervision, Validation, Writing – original draft, Writing – review and editing.

Conflicts of interest

There are no conflicts to declare.

Data availability

The data that support the findings of this study are openly available in ESRF data portal at https://doi.esrf.fr/10.15151/ESRF-ES-2166874660.

Acknowledgements

The authors acknowledge financial support from the SUSTBATT project (M-ERA.NET, Project No. 337463), funded by the Research Council of Norway (Project No. 315947). This work was also supported by Grant No. PCI2022-132993, funded by MCIN/AEI/10.13039/501100011033 and by the European Union "NextGenerationEU"/PRTR. Support from the Research Council of Norway to NORTEM (Project No. 197405) is also gratefully acknowledged. Beamtime at BM01 (SNBL), ESRF, through experiment MA-6477, is acknowledged. The authors thank The Swedish Algae Factory for providing the diatom SiO_2 material.

View Article Online
DOI: 10.1039/D6TA02278B

Notes and references

1 Precedence Research, *Silicon Anode Battery Market Size to Hit USD 20,799.74 Million by 2034*, https://www.precedenceresearch.com/silicon-anode-battery-market.

2 R. Zope, *Silicon Anode Battery Market Size, Share & Analysis, 2032*, https://www.persistencemarketresearch.com/market-research/silicon-anode-battery-market.asp.

3 Market.us, *Silicon Anode Battery Market*, https://market.us/report/global-silicon-anode-battery-market/.

4 M. N. Obrovac and L. Christensen, *Electrochemical and Solid-State Letters*, 2004, **7**, A93.

5 P. Schweigart, W. Hua, P. A. Sánchez, C. Lian, I. Nylund, D. Wragg, S. Y. Lai, F. Cova, A. M. Svensson and M. V. Blanco, *Small*, 2025, **21**, 2406615.

6 P. Alonso-Sánchez, W. Hua, K. Thangaian, P. E. Vullum, J. T. A. Karlsen, A. M. Svensson, F. Vullum-Bruer, J. Campo, F. Cova and M. V. Blanco, *Small*, 2025, **21**, e2504704.

7 M. Gautam, G. K. Mishra, K. Bhawana, C. S. Kalwar, D. Dwivedi, A. Yadav and S. Mitra, *ACS Applied Materials & Interfaces*, 2024, **16**, 45809–45820.

8 E. Kim, H. An, I. Kang, C. Lee, M. An, S. Chae and Y. Son, *Journal of Power Sources*, 2025, **632**, 236314.

9 M. V. Blanco and M. R. Palacin, *Journal of Materials Chemistry A*, 2025, **13**, 21421–21435.

10 N. Liu, K. Huo, M. T. McDowell, J. Zhao and Y. Cui, *Scientific Reports*, 2013, **3**, 1919.

11 J. Liu, P. Kopold, P. A. van Aken, J. Maier and Y. Yu, *Angewandte Chemie International Edition*, 2015, **54**, 9632–9636.

12 M. V. Blanco, V. Renman, F. Vullum-Bruer and A. M. Svensson, *RSC Advances*, 2020, **10**, 33490–33498.

13 K. Thangaian, W. Hua, J. T. Aga Karlsen, I.-E. Nylund, S. Nilsson, T. Ericson, M. Hahlin, A. M. Svensson and M. V. Blanco, *ACS Sustainable Resource Management*, 2024, **1**, 767–777.

14 W. Hua, P. E. Vullum, K. N.-N. Hjelseng, J. Hamonnet, P. Alonso-Sánchez, J. Zhu, Z. Hegedüs, J. R. Zuazo, F. Cova, A. M. Svensson and M. V. Blanco, *Energ & Environmental Materials*, 2025, **8**, e70074.

15 W. Hua, I.-E. Nylund, F. Cova, A. M. Svensson and M. V. Blanco, *Scientific Reports*, 2023, **13**, 20447.

16 K. Thangaian, A. Gaarud, I.-E. Nylund and M. V. Blanco, *ACS Sustainable Resource Management*, 2024, **1**, 2284–2293.

17 B. Campbell, R. Ionescu, M. Tolchin, K. Ahmed, Z. Favors, K. N. Bozhilov, C. S. Ozkan and M. Ozkan, *Scientific Reports*, 2016, **6**, 33050.

18 J. R. Szczech and S. Jin, *Energy & Environmental Science*, 2011, **4**, 56–72.

19 N. Wan, L. Wang, S. Li, L. Shen, F. Xi, J. Lu, Z. Tong, X. Chen and W. Ma, *Small*, 2026, **22**, 2412705.

20 N. Kim, H. Park, N. Yoon and J. K. Lee, *ACS Nano*, 2018, **12**, 3853–3864.

21 A. Darghouth, S. Aouida and B. Bessais, *Silicon*, 2021, **13**, 667–676.

22 Z. Lin, P. Sun, C. Zhou and Z. Z. Fang, *ACS Omega*, 2025, **10**, 473–483.

23 T. Autthawong, O. Namsar, A. Yu and T. Sarakonsri, *Journal of Materials Science: Materials in Electronics*, 2020, **31**, 9126–9132.

24 L. A. September, N. Kheswa, N. S. Seroka and L. Khotseng, *RSC Advances*, 2023, **13**, 1370–1380.

25 A. Gaarud, K. Thangaian, P. Alonso-Sánchez and M. V. Blanco, *Advanced Sustainable Systems*, 2025, **9**, 2500117.

26 X. Li, P. Yan, B. W. Arey, W. Luo, X. Ji, C. Wang, J. Liu and J.-G. Zhang, *Nano Energy*, 2016, **20**, 68–75.

27 K. Thangaian, T. Ericson, P. E. Vullum, P. Alonso-Sánchez, A. C. Svarverud, A. M. Svensson, F. Vullum-Bruer, M. Hahlin and M. V. Blanco, *Journal of Power Sources*, 2025, **641**, 236837.

28 W. Choi, J. Bae, H. Kim, C. Son, M. Karuppaiah and J. K. Lee, *Electrochimica Acta*, 2024, **498**, 144687.

29 W. C. Cho, H. J. Kim, H. I. Lee, M. W. Seo, H. W. Ra, S. J. Yoon, T. Y. Mun, Y. K. Kim, J. H. Kim, B. H. Kim, J. W. Kook, C.-Y. Yoo, J. G. Lee and J. W. Choi, *Nano Letters*, 2016, **16**, 7261–7269.

30 B. Zhang, F. Wang, J. Chen, B. Li, K. Liu and Q. Han, *Silicon*, 2022, **14**, 8409–8416.

31 P. Alonso Sánchez, K. Thangaian, O. A. Øie, A. Gaarud, M. Rodríguez Gomez, V. Diadkin, J. Campo, F. H. Cova and M. V. Blanco, *ACS Applied Energy Materials*, 2025, **8**, 2249–2259.

32 N. Lin, Y. Han, J. Zhou, K. Zhang, T. Xu, Y. Zhu and Y. Qian, *Energy & Environmental Science*, 2015, **8**, 3187–3191.

33 J. Niu, D. Shen, Z. Ren, R. Zhang, D. Xia, Y. Yang, W. Dong and S. Yang, *ChemistrySelect*, 2025, **10**, e02379.

34 M. Cai, Z. Zhao, J. Qu, Q. Ma, X. Qu, L. Guo, H. Xie, D. Wang and H. Yin, *Journal of Materials Chemistry A*, 2021, **9**, 21323–21331.

35 Z. Zhao, M. Cai, H. Zhao, Q. Ma, H. Xie, P. Xing, Y. X. Zhuang and H. Yin, *ACS Sustainable Chemistry & Engineering*, 2022, **10**, 5035–5042.

36 Z. Zhao, M. Cai, Y. Zhao, H. Xie, Y. X. Zhuang and H. Yin, *ACS Applied Nano Materials*, 2023, **6**, 502–511.

37 X. Lin, A. Li, D. Li, H. Song and X. Chen, *ACS Applied Materials & Interfaces*, 2020, **12**, 15202–15210.

38 N. Lin, Y. Han, L. Wang, J. Zhou, J. Zhou, Y. Zhu and Y. Qian, *Angewandte Chemie International Edition*, 2015, **54**, 3822–3825.

39 M. Je, J. C. Kim, J. Kim, S. Kim, S. Ryu, J. Ryu, S. K. Kwak and S. Park, *Advanced Science*, 2025, **12**, 2412239.

40 Z.-W. Zhou, Y.-T. Liu, X.-M. Xie and X.-Y. Ye, *Chemical Communications*, 2016, **52**, 8401–8404.

41 X. Wan, Z. Tang, J. Chen, Y. Xue, J. Zhang, X. Guo, Y. Liu, Q. Kong, A. Yuan and H. Fan, *Chemistry Letters*, 2019, **48**, 1547–1550.

42 C.-H. Zheng, G.-P. Zhang, S.-S. Wang, A.-Q. Mao and D.-L. Fang, *Journal of Alloys and Compounds*, 2021, **875**, 159974.

43 K. P. Marshall, H. Emerich, C. J. McMonagle, C. A. Fuller, V. Dyadkin, D. Chernyshov and W. v. Beek, *Journal of Syn-*

View Article Online
DOI: 10.1039/D6TA02278B

chrotron Radiation, 2023, **30**, 267–272.

44 C. Prescher, and V. B. Prakapenka, *High Pressure Research*, 2015, **35**, 223–230.

45 O. Arcelus, J. Rodríguez-Carvajal, N. A. Katcho, M. Reynaud, A. P. Black, D. Chatzogiannakis, C. Frontera, J. Serrano-Sevillano, M. Ismail, J. Carrasco, F. Fauth, M. R. Palacin and M. Casas-Cabanas, *Journal of Applied Crystallography*, 2024, **57**, 1676–1690.

46 P. Alonso, M. V. Blanco and E. H. Swensen, *In-situ one-pot synthesis of SiOx/C anodes by SAXS/WAXS measurements*, 2028, https://doi.esrf.fr/10.15151/ESRF-ES-2166874660.

47 G. Song, J. Ryu, J. C. Kim, J. H. Lee, S. Kim, C. Wang, S. K. Kwak and S. Park, *Communications Chemistry*, 2018, **1**, 42.

48 J. Ryu, J. H. Seo, G. Song, K. Choi, D. Hong, C. Wang, H. Lee, J. H. Lee and S. Park, *Nature Communications*, 2019, **10**, 2351.

49 M.-A. Einarsrud, H. Justnes, E. Rytter and H. Øye, *Polyhedron*, 1987, **6**, 975–986.

50 M. Khan, X. Ding, H. Zhao, Y. Wang, N. Zhang, X. Chen and J. Xu, *Journal of Electronic Materials*, 2022, **51**, 3379–3390.

Data Availability Statement

View Article Online
DOI: 10.1039/D6TA02278B

The data that support the findings of this study are openly available in ESRF data portal at **https://doi.esrf.fr/10.15151/ESRF-ES-2166874660**.